ALGERIAN JOURNAL OF ENGINEERING AND TECHNOLOGY

Algerian Journal of Engineering and Technology
ISSN: 2716-9227 (Print)
EISSN: 2716-9278 (Online)
DOI:
Sahli et al / vol. 10, n°2 - 2025

Original Article Open Access

Multi-parametric study of welding parameters on the durability of CANDU fuel assemblies

Sahli Amane[a]*, Bouderhem Nourelislam[b], Sadouki Mohamed[a], Menchi Omar[a], Belkacem Rabah Ahmed Walid[a], Mekideche Sofiane[a] and Djema Oussama[c].

[a]*Nuclear Research Center of Draria CRND, Algiers, Algeria; a-sahli@crnd.dz*
[b]*National Polytechnic School of Algiers ENP, Algiers, Algeria; nourelislam.bouderhem@g.enp.edu.dz*
[c]*Research Centre in Semiconductors Technology for Energetics CRTSE; Algiers, Algeria; oussama.djema@g.enp.edu.dz*
* *Corresponding author.* E-mail address: a-sahli@crnd.dz
Article history: Received 01 September 2025, Revised 29 September 2025, Accepted 05 October 2025

ABSTRACT

This study focuses on TIG (Tungsten Inert Gas) welding of Zircaloy-4, used in fuel rod assemblies for CANDU (Canada Deuterium Uranium) reactors, to analyze the effect of welding parameters on the microstructural and mechanical quality of end-plug-to-cladding joints. Despite the extensive use of TIG welding for Zircaloy-4, understanding the induced metallurgical phenomena that affect mechanical properties remains a major challenge. This study aims at systematic characterization of welding parameter effects on microstructure and properties of plug-cladding joints, identifying metallurgical zones and correlating operating conditions with final performance. Welds were produced under various conditions of current intensity and rotation speed and examined using optical microscopy, Scanning Electron Microscopy (SEM), X-ray Diffraction (XRD), Vickers microhardness, and hydraulic burst tests. The analysis revealed three distinct zones: fusion zone (FZ), heat-affected zone (HAZ), and base metal (BM) with typical Widmanstätten structures. A clear correlation was found between heat input, hardness, and mechanical strength. Hydraulic burst tests confirmed the high performance of optimized welds, showing failure stresses of approximately 425 ± 10 MPa.

Keywords: TIG welding, Zircaloy-4, Fuel rod assemblies, CANDU, Fusion zone, Heat-affected zone, Widmanstätten structures, Burst test.

Graphical abstract

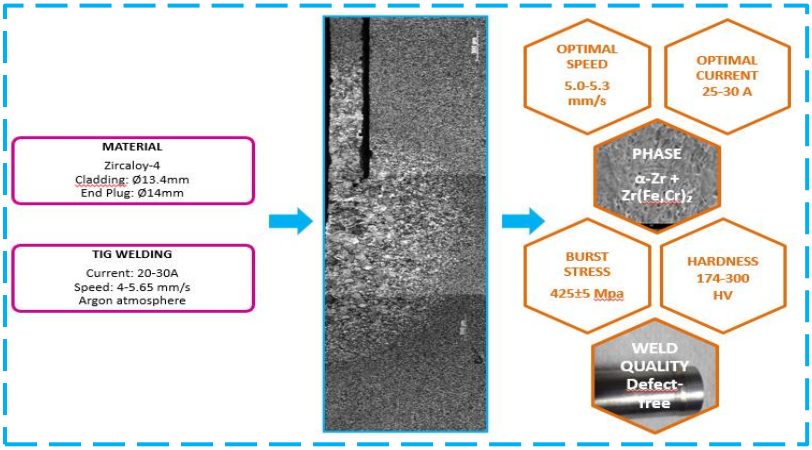

Recommended Citation
Sahli A, Bouderhem N, Sadouki M, Menchi O, Belkacem Rabah A W, Mekideche S and Djema O. Multi-parametric study of welding parameters on the durability of CANDU fuel assemblies. *Alger. J. Eng. Technol. 2025, 10(2): 74-86*

1. Introduction

The nuclear industry relies on a fundamental principle: the absolute integrity of fuel assemblies. This requirement becomes particularly critical for CANDU reactors, which use pressurized heavy water as moderator and coolant [1]. These reactors utilize fuel elements consisting of tubular rods manufactured from zirconium alloys, exceptional materials selected for their remarkable neutronic properties. Zirconium alloys, including Zircaloy-4, are well known for their remarkable combination of properties : a very low neutron capture cross-section (around 0.18 barn) [2], excellent corrosion resistance in high-temperature aqueous environments, and outstanding mechanical strength under the severe stresses of the reactor core. [2]. These properties make it the material of choice for the most demanding nuclear applications. The design of CANDU fuel elements is based on a meticulous assembly of Zircaloy-4 tubular cladding, hermetically sealed by end plugs. This tight closure represents far more than a simple mechanical assembly: it constitutes the primary containment barrier, the ultimate guardian against any dispersion of radioactive material into the reactor environment. TIG welding is the process of choice for producing these critical assemblies. This method is distinguished by its unique ability to generate high-quality joints, characterized by their exemplary reproducibility and controlled heat input [3]. This latter property proves essential for preserving the metallurgical integrity of zirconium, a material particularly sensitive to thermal transformations.

Echol's research on post-weld heat treatments revealed that treatments at 800°C for 1 hour successfully restore ductility in TIG-welded joints, increasing total elongation from 12.4% to 16.5%, while prolonged exposure beyond 18 hours induces detrimental blocky α formation in the HAZ zone [4]. Furthermore, Loucif's investigation of β quenched Zircaloy-4 aging characterized five distinct microstructural transformation stages between 100°C and 750°C, including Fe and Cr precipitation and recrystallization processes, defining essential time-temperature relationships that govern phase stability and mechanical response. These investigations emphasize the sensitivity of Zircaloy-4 microstructure to thermal history and highlight the importance of controlled thermal processing to ensure weld quality and service performance. [5].

Despite its extensive use, fine understanding of the metallurgical phenomena induced by TIG welding of Zircaloy-4 remains a major scientific challenge. Complex thermal cycles, α↔β phase transformations, and resulting microstructural evolutions directly influence the mechanical properties [6] and durability of assemblies. This study aims to improve understanding of the process by systematically characterizing the effect of welding parameters on the microstructure and mechanical properties of plug-cladding joints. Particular attention is paid to identifying different metallurgical zones, characterizing formed structures, and establishing correlations between operating conditions and final performance.

2. Materials and Methods

2.1. Material

The Zircaloy-4 used in this study was in the form of rods of 14 mm diameter for the end plugs and tubes with outer diameter of 13.4 ± 0.3 mm and inner diameter of 12.3 mm for the cladding. The chemical composition was verified by X-ray fluorescence spectrometry and compared to the requirements of ASTM B353 standard Grade R60804 [7]. The analysis results reveal an overall compliant composition with the main alloying elements: Sn 1.54%, Fe 0.142%, Cr 0.231%, and Zr 97.79%. Two notable anomalies were identified: a chromium content slightly above the specified maximum limit of 0.13%, and the unexpected presence of vanadium at approximately 0.228%. These deviations could be explained by local material heterogeneity or by the precision limitations of the XRF method employed.

The 50 cm long cladding tubes were cut into 5 to 10 cm segments using a precision cut-off machine. The end plugs were machined from 14 mm diameter rods. Meticulous cleaning with acetone was performed on all components to remove grease residues and other impurities that could affect weld quality.

2.2. TIG Welding Process

Welding was performed on automatic equipment specifically designed for end-plug-to-cladding assemblies, as shown in Figure 1. The system includes a welding chamber under controlled atmosphere, a vacuum-gas system for evacuation to 0.04 mbar and argon injection, a rotation motor to rotate the sample, and a current source for TIG welding. The electrode used is 2% thoriated tungsten with a diameter of 2.4 mm, with an arc length maintained at approximately 1 mm. Six series of welds were produced with variable parameters listed in Table 1 to evaluate the influence of current intensity of 20 A and 30 A and rotation speed between 4.04 and 5.65 mm/s on the final quality of the assemblies.

Fig 1. Automatic TIG welding system showing the welding chamber, rotation motor, and controlled atmosphere setup.

Table 1. Applied welding parameters

N°	Intensity (A)	Time (s)	Rotation speed (mm/s)
01	25	10	4,04
02	30	7	5,65
03	30	8,5	5,05
04	30	7,5	5,25
05	25	8	5,05
06	20	7	5,65

2.3 Microstructural Characterization

Axial sections were cut from the welded samples and cold-mounted in epoxy resin. Mechanical polishing was carried out using abrasive papers of decreasing grit size (180 to 4000), followed by fine polishing with 3 µm and 1 µm diamond pastes. Chemical etching was performed with a solution of 3% HF, 47% HNO3, and 50% distilled water to reveal the microstructure. For macrographic examination, two etchants were used: 40% HF and aqua regia (1 part distilled water, 1

part HNO3 at 69%, and 2 parts HCl at 37%). Etching was applied for 2 minutes to highlight the different zones of the weld bead.

Microstructural observations were performed using a Carl Zeiss Axio Tech 100 optical microscope and a ZEISS Gemini SEM 300 scanning electron microscope equipped with an EDS microanalysis system for local elemental composition identification.

XRD analysis was carried out using a PHILIPS X'PERT PRO MPD diffractometer with CuKα radiation (λ = 1.540598 Å) at 30 kV and 40 mA. Diffraction spectra were recorded in the 2θ range of 20°–100°, with a step size of 0.02° and an acquisition time of 350 s per step.

2.4 Mechanical Characterization

Microhardness measurements were performed using a Vickers MHT-10 Paar Physica microhardness tester across all weld zones (BM, HAZ, and FZ). A load of 100 gf was applied for 15 seconds, with indents spaced 200 μm apart along the transverse section. Burst test specimens of 150 mm in length were prepared with flared ends. The internal water pressure was gradually increased at a rate of 140 ± 15 bar/min until failure.

The burst stress was calculated using the formula:

$$\sigma = \frac{P \times D_i}{2t} \qquad (1$$

Where P is the burst pressure, D_i the inner diameter, and t the wall thickness. The circumferential strain was determined by measuring the diameter before and after testing.

3. Results and Discussion

3.1 Visual Inspection and Weld Quality

Visual inspection of the six weld series revealed several typical defects associated with inappropriate selection of welding parameters. Table 2 presents the different defects observed corresponding to the parameter settings defined in Table 1.

Table 2. Visual defects identified in the six weld series

Weld	Defects	Observations
No. 1		The weld bead does not uniformly cover the entire circumference of the joint. This defect results from insufficient welding current, which prevents full fusion of the base metal.
No. 2		The use of a high current combined with a high travel speed produced a circular crater at the end of the weld bead. This defect is typical of excessively rapid cooling.
No. 3 and 5	 	Regular, homogeneous, and defect-free weld beads were observed, representing the optimal parameters for this type of assembly.
No. 4	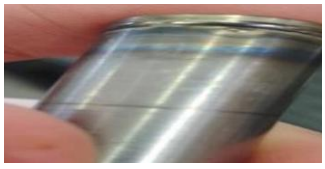	Excessive reinforcement due to the combination of a 30 A current and a travel speed of 5.25 mm/s resulted in an excessive buildup of molten metal.
No. 6	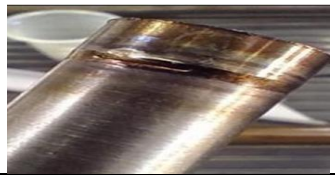	Poor weld caused by the condition of the cladding end plug interface (manufacturing defect in the tube and plug).

3.2 Macrographic Characterization

Figure 2 presents the macrographic examination of the cross-sections, clearly revealing three distinct characteristic zones. The FZ represents the central region where the metal has completely melted and subsequently solidified, with its width and depth varying directly with the heat input according to [8] :

$$Q = \frac{I \times U}{V} \quad (2$$

Where Q is the heat input, I is the welding current, U is the arc voltage, and V is the welding speed.

The HAZ is the peripheral region where the base metal has undergone metallurgical transformations without complete melting, and its extent strongly depends on thermal diffusion and welding parameters. The BM is the unaffected area that retains the original microstructure of the material.

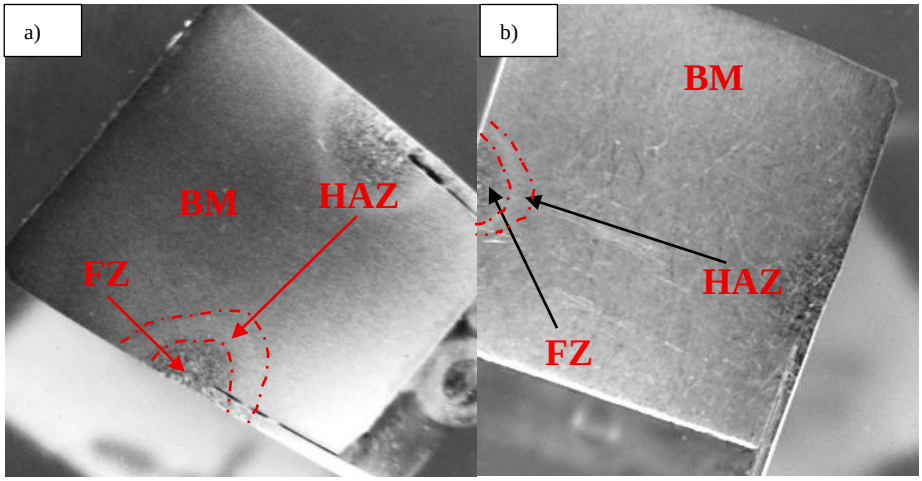

Fig 2. Macrographic examination of TIG welds on Zircaloy-4

Figure 2a presents a comparison of two samples with different parameters, clearly showing the influence of heat input. An increase in current intensity at constant travel speed results in a proportional increase in power input, leading to a wider and deeper fusion zone and a larger HAZ. This observation confirms the fundamental relationship: the higher the heat input, the greater the extent of the affected zones.

3.3 Microstructural Analysis

Microscopic observation reveals a marked difference between the microstructure of the base metal of cladding and that of the end plug:

- Cladding: Exhibits very fine grains highly elongated in a single direction, resulting from the rolling process. This controlled plastic deformation generates a characteristic fibrous structure with grains preferentially oriented along the rolling axis.
- End plug: Shows larger grains with equiaxed morphology, typical of material obtained by machining without significant plastic deformation. The absence of work hardening explains the larger grain size.

Figure 3 presents the difference in grain size, which directly translates into microhardness variation in accordance with the Hall – Petch law [9]:

$$\sigma_c = \sigma_0 + \frac{k}{\sqrt{d}} \qquad (3$$

Where σc is the yield stress, σ0 is the friction stress representing the intrinsic resistance of the crystal lattice, k is the Hall–Petch slope, and d is the average grain diameter

The cladding, with its fine grains, exhibits a higher hardness of 233 HV compared to the end plug at 174 HV.

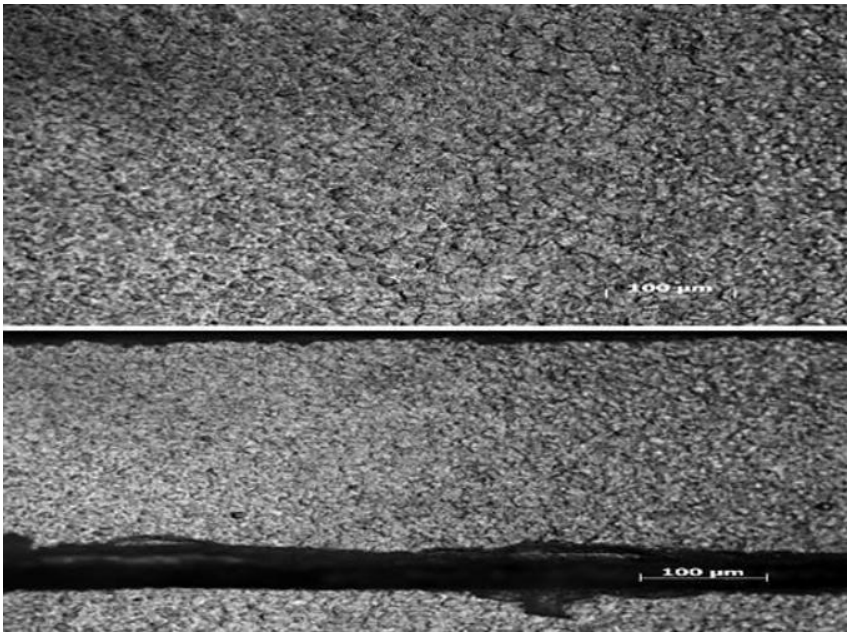

Fig 3. Microstructure of the base metal of the plug and the cladding

Figure 4 presents SEM analysis coupled with EDS, revealing the presence of intermetallic precipitates of the $Zr(Fe,Cr)_2$ type, known as Laves phases [2,10]. These particles, with a hexagonal structure, appear as bright spots dispersed within the α-Zr matrix. Spot EDS analysis on these precipitates indicates locally elevated iron and chromium contents, confirming their chemical nature.

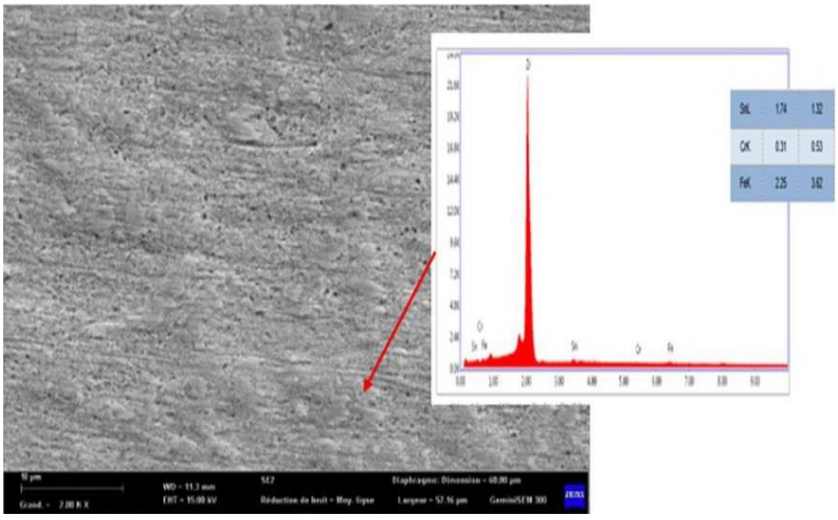

Fig 4. SEM micrography of the base metal and EDS analysis of an intermetallic compound

Figure 5 presents the HAZ, which exhibits a gradually modified microstructure depending on the maximum temperature reached during welding. Several sub-zones can be distinguished:

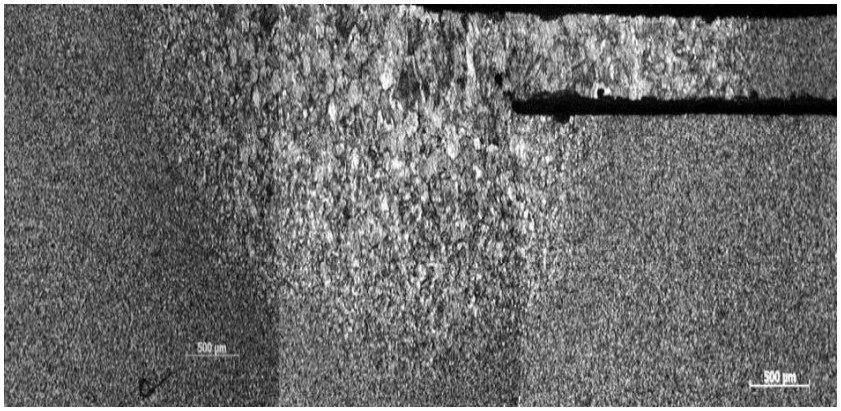

Figure 5. Cross-sectional micrograph of a Zircaloy-4 cladding-plug assembly welded by TIG

- Sub-critical zone (450-810°C) [11]: No complete phase transformation. Slight recrystallization of cladding grains (partial refinement) and initial grain coarsening of the end plug are observed. This zone exhibits intermediate microhardness of approximately 206 HV.
- Intercritical zone (810-980°C): Partial α→β transformation followed by return to α during cooling. This zone is characterized by the appearance of Widmanstätten structures [8,12], consisting of fine lamellae of α phase organized according to preferential crystallographic orientations. The formation of these structures results from diffusion-controlled phase transformation during relatively slow cooling. Microhardness progressively increases to reach 230-250 HV.
- Overheating zone : Grains become very large due to exposure to high temperatures close to the fusion zone. Depending on cooling rate and presence of pinning particles, either a basket weave structure or parallel lamellae are observed [14]. This zone exhibits the highest hardness values (271-290 HV) due to the fine lamellar structure formed.

The FZ represents the weld core where the metal completely melted and then solidified. Microscopic observation reveals:

- Solidification structure: Very elongated columnar grains oriented perpendicular to the fusion interface, growing in the direction of maximum thermal gradient. This morphology is typical of directional solidification [13].
- Widmanstätten structures: Marked presence of α lamellae organized according to specific crystallographic orientations within former β grains. These structures result from β→α transformation during post-welding cooling.
- Maximum microhardness: The fusion zone exhibits the highest microhardness values of the entire assembly (>300 HV locally, average 271-290 HV). This high hardness is explained by several factors: (1) complete α→β→α phase transformation, (2) formation of fine lamellar structure, (3) presence of residual stresses, and (4) local microstructure refinement.

The Widmanstätten structures observed in the HAZ and FZ deserve particular attention. These characteristic formations develop during β→α transformation and consist of platelets or lamellae of α phase precipitating according to preferential crystallographic planes of the parent β phase. Their formation obeys the Burgers orientation relationships : {0001}α // {110}β and <11$\bar{2}$0>α // <111>β. The fineness of these lamellae depends essentially on cooling rate: rapid cooling generates fine lamellae (increasing hardness), while slow cooling produces coarse lamellae. Figure 6 presents relatively fine structures, indicating moderate to rapid cooling rates. These structures significantly influence mechanical properties: they increase strength and hardness but can also reduce ductility and promote crack propagation along certain crystallographic orientations [14,15].

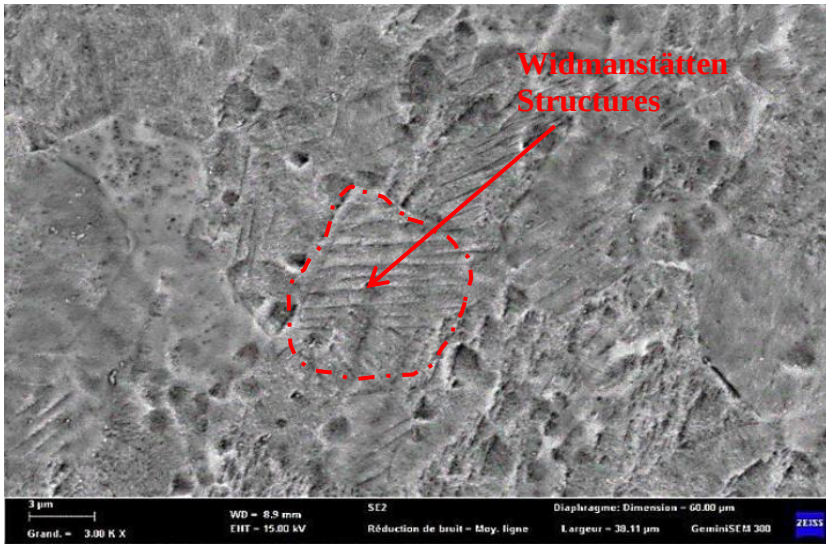

Fig 6. SEM observation at 3000x of the HAZ and Widmanstätten Structures

3.4 X-Ray Diffraction Analysis

Figure 7 presents the diffractogram obtained on the welded Zircaloy-4 alloy, which reveals:

- Dominant α-Zr phase: High-intensity peaks located at 2θ°, 35° and 37° correspond to the characteristic crystallographic planes of the hexagonal α-Zr phase [2,12]. The high intensity of these reflections confirms that this phase constitutes the major structural component of the sample, both in the base metal and in the welded zones after complete cooling.
- Intermetallic precipitates $Zr(Fe,Cr)_2$: Several low-intensity peaks appear at 2θ°, 38°, 50°, 70°, and 80°, attributable to the Laves-type intermetallic phase $Zr(Fe,Cr)_2$. The low intensity of these reflections indicates a minor volume fraction, estimated between 1 and 3%. These precipitates play an important role in improving corrosion resistance and controlling grain size [2,6].
- Absence of residual β phase: No peak corresponding to the β phase (body-centered cubic) is detected, confirming complete β→α transformation during post-welding cooling. The α↔β transformation temperature for Zircaloy-4 is around 810-863°C depending on local composition and heating/cooling rate [2].

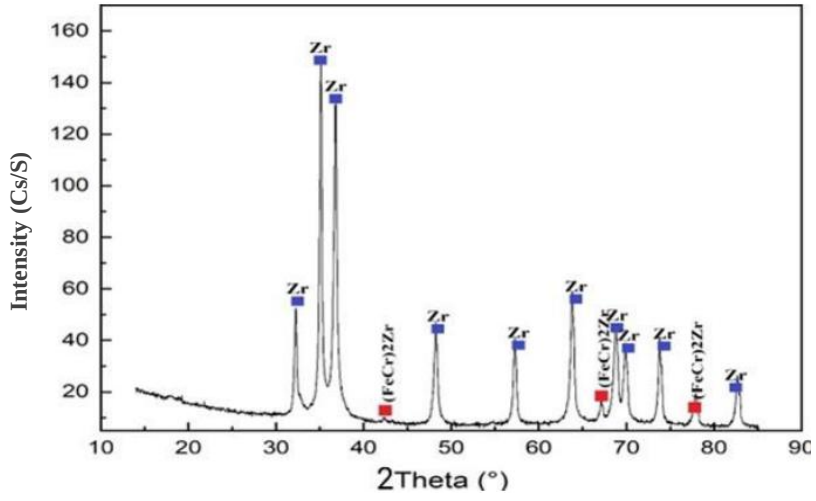

Fig 7. X-ray diffraction pattern of Zircaloy-4 alloy

Quantitative analysis of peak widths suggests a heterogeneous distribution of residual micro-strains, which are more significant in the fusion zone and HAZ than in the base metal [4,16]. These strains result from thermal gradients during welding and differences in thermal expansion coefficient between phases.

3.5 Microhardness Profile

Figure 8 presents the transverse microhardness profile, revealing a characteristic evolution across the different weld zones and allowing quantification of the heat treatment effect induced by welding:

- Zone 1 : Base metal on end plug side (6000-7200 µm): Minimum microhardness of 174 ± 8 HV. This low hardness is explained by the absence of work hardening and relatively coarse grain size (50-80 µm). The material exhibits a recrystallized equiaxed structure without significant residual stresses.
- Zone 2 : HAZ on end plug side (4500-6000 µm): Progressive increase up to 206 ± 10 HV. This elevation results from two phenomena: partial recrystallization inducing slight grain refinement, and homogenization of internal stresses. The maximum temperature reached in this zone is estimated between 500 and 750°C.
- Zone 3 : Transition zone (2000-4500 µm): Marked increase reaching 230-250 HV. This zone corresponds to intercritical temperatures (810-980°C) where partial α↔β phase transformations occurred. The transient presence of β phase, harder than α phase, and the formation of Widmanstätten structures explain this increase [4,16].
- Zone 4 : Weld core / Fusion zone (800-2000 µm): Maximum values locally exceeding 300 HV (average 271-290 HV). This exceptional hardness is explained by: complete α→β→α phase transformation, fine lamellar Widmanstätten structure, high dislocation density, fine precipitation of intermetallic phases, and significant residual stresses due to thermal gradients. The maximum temperature in this zone exceeded the local melting point (1850°C) [2].
- Zone 5 : Base metal on cladding side (0-800 µm): Microhardness of 233 ± 12 HV, significantly higher than the end plug. This fundamental difference is explained by the cladding manufacturing process, cold rolling followed by partial annealing, which generates residual work hardening and a fibrous structure with fine elongated grains (length 100-150 µm, width 10-20 µm).

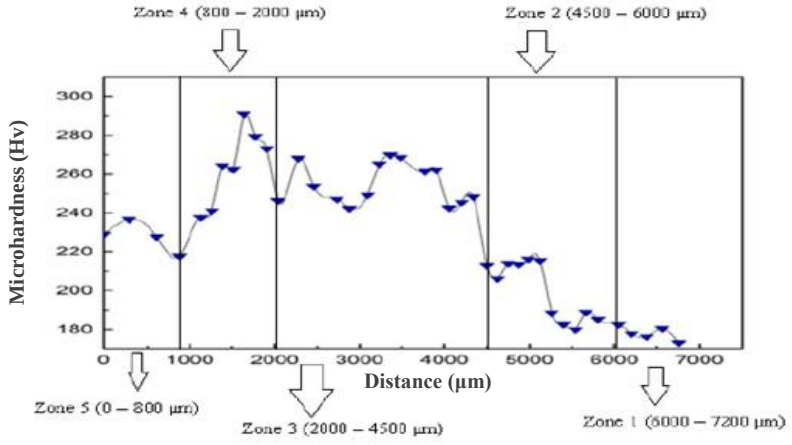

Fig 8. Microhardness profile of a TIG welding specimen as function as distance

Hardness gradient and mechanical implications: The observed hardness gradient (126 HV between extreme zones) creates mechanical heterogeneity that can influence in-service behavior: stress concentration at interfaces between zones of different hardness, preferential crack propagation in softer zones, and localized plastic deformation under loading [17]. Nevertheless, this gradient is inevitable in any fusion welding process and remains acceptable if its magnitude and spatial extent are controlled. The relationship between heat input and hardness is clearly established: the higher the heat input, the

more extensive the high hardness zone (FZ + inner HAZ), confirming the importance of precise welding parameter control.

3.6 Hydraulic Burst Test

The hydraulic burst test constitutes a functional test simulating the extreme pressurization conditions that the fuel assembly may experience in service. Figure 9 presents the obtained results, revealing mechanical behavior in three distinct phases:

- Elastic rise (0-300 s): Linear increase in hoop stress with internal pressure, reflecting reversible elastic deformation of the material according to Hooke's law. The apparent modulus can be estimated from the slope of this portion.
- Creep plateau (300-450 s): Stabilization of stress around 420-430 MPa corresponding to the plastic yield limit of the material. In this phase, the tube undergoes progressive plastic deformation (primary and secondary creep) with gradual wall thinning. Pressure continues to increase but stress stabilizes because wall thinning partially compensates for the pressure increase.
- Rupture (450 s): Abrupt drop in stress marking catastrophic tube failure. The ultimate stress reached (430 MPa) significantly exceeds the conventional yield strength of Zircaloy-4 (240-310 MPa depending on metallurgical state), confirming significant work hardening capacity before rupture [18].

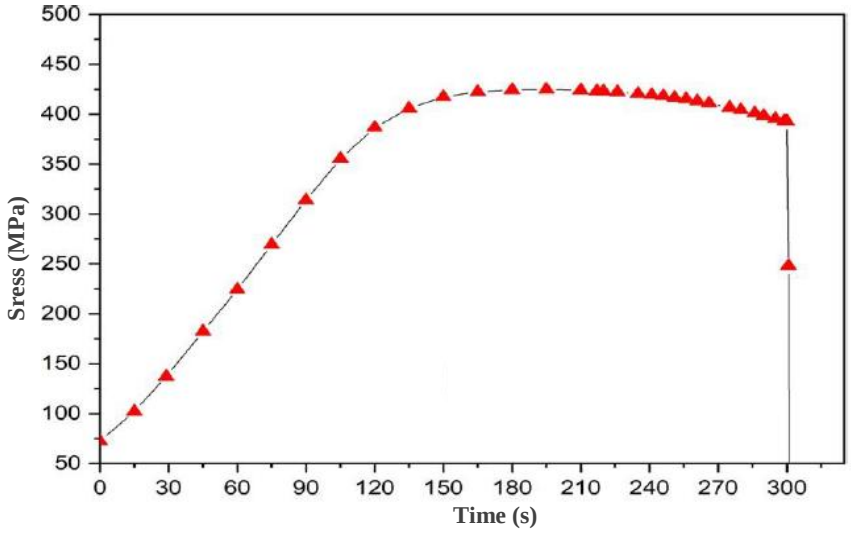

Fig 9. Stress evolution as a function of time during the burst test

Figure 10 presents the visual post-burst examination, revealing a clear longitudinal crack oriented along the tube axis. This morphology is characteristic of ductile rupture by exceeding maximum hoop stresses. The crack propagated perpendicular to the principal stresses in tangential direction, in accordance with classical tube rupture mechanisms under internal pressure [19]. The crack edges exhibit significant localized plastic deformation, confirming the ductile nature of the rupture. No violent fragmentation is observed, indicating good material capacity to absorb deformation energy before final failure.

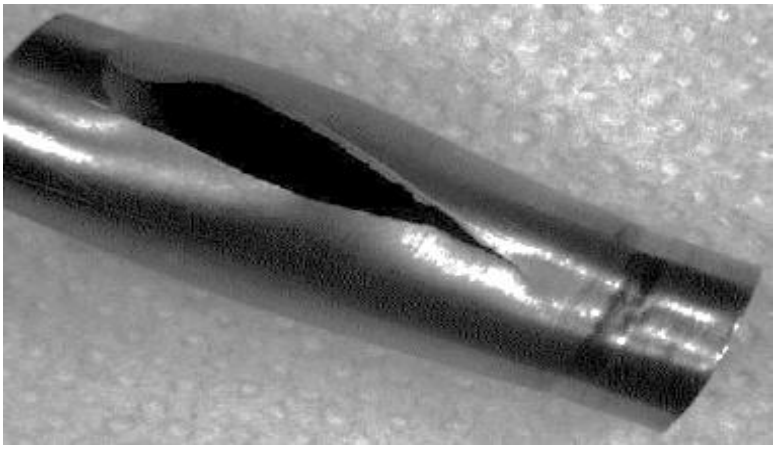

Fig 10. Specimen morphology after burst

Crack initiation does not appear preferentially localized in the welded zone, suggesting that the optimized weld possesses strength at least equivalent to the base metal. This result validates the metallurgical quality of assemblies produced with the identified optimal parameters (samples 03 and 05).

Post-burst measurement of diameter reveals permanent hoop deformation of approximately 15-20%, a value characteristic of significant ductility. This deformation, although highly localized at the rupture zone, confirms the capacity of Zircaloy-4 to accommodate significant plastic deformations before failure [17]. The rupture stress obtained (430 MPa) is consistent with values reported in the literature for Zircaloy-4 in recrystallized condition (400-550 MPa depending on crystallographic orientation and surface condition) [19]. This performance validates the conformity of welds to mechanical requirements of the nuclear field.

4. Conclusion

This study on TIG welding of Zircaloy-4 end plug to cladding assemblies for nuclear applications demonstrates that current intensity and rotation speed are critical parameters governing weld quality. Optimal welding conditions of 25-30 A current intensity and 5-5.3 mm/s rotation speed consistently produce defect-free, homogeneous welds. Microstructural characterization reveals distinct zones featuring Widmanstätten structures that directly influence mechanical properties, with microhardness values ranging from 174 HV in the base metal to 300 HV in the fusion zone. Hydraulic burst testing validated the exceptional mechanical performance of optimized welds, achieving rupture stresses of 425±5 MPa that significantly exceed operational requirements for CANDU fuel assemblies. These findings confirm that properly optimized TIG welds satisfy rigorous nuclear industry standards, ensuring both structural integrity and long-term reliability in reactor service conditions.

Funding Support

This research received no external funding.

Ethical Statement

This study does not contain any studies with human or animal subjects performed by any of the authors.

Conflict of Interest

The authors declare that they have no conflict of interest.

Data Availability Statement

Not applicable.

References

1. International Atomic Energy Agency (IAEA). Assessment and Management of Ageing of Major Nuclear Power Plant Components Important to Safety: CANDU Reactor Assemblies; IAEA-TECDOC-1197; IAEA: Vienna, Austria, 2001.
2. Lemaignan, C.; Motta, A.T. Zirconium Alloys in Nuclear Applications. *Mater Sci Technol*. 1994, 10, 1–51.
3. Rudling, P.; Strasser, A.; Garzarolli, F.; van Swam, L. Welding of Zirconium Alloys; IZNA7 Special Topic Report; Advanced Nuclear Technology International: Molnlycke, Sweden, 2007.
4. Echols, J.; Garrison, L.; Silva, C.; Lindquist, E. Temperature and Time Effects of Post-Weld Heat Treatments on Tensile Properties and Microstructure of Zircaloy-4. *J Nucl Mater*. 2021, 551, 152952.
5. Loucif, K.; Borrelly, R.; Merle, P. Microstructural Evolution of β-Quenched Zircaloy-4 During Agings Between 100 and 750°C. *J Nucl Mater*. 1994, 210, 84–96.
6. Lemaignan, C. Physical Phenomena Concerning Corrosion under Irradiation of Zr Alloys. *Compr Nucl Mater.* 2012, 2.07, 217–232.
7. ASTM B353-00. Standard Specification for Wrought Zirconium and Zirconium Alloy Seamless and Welded Tubes for Nuclear Service; ASTM International: West Conshohocken, PA, USA, 2000.
8. Tao, W.; Cai, C.; Li, L.; Chen, Y.; Wang, Y.L. Pulsed Laser Spot Welding of Intersection Points for Zircaloy-4 Spacer Grid Assembly. *Mater Des*. 2013, 52, 487–494.
9. Hansen, N. Hall–Petch Relation and Boundary Strengthening. *Scr Mater.* 2004, 51, 801–806.
10. Zhang, Z.; Wang, Z.; Yao, B.; Hao, Z.; Xie, Y.; Chai, G.; Fan, W.; Tan, H.; Lin, X. Microstructure and High-Temperature Mechanical Properties of a Nuclear Zircaloy-4 Alloy Fabricated by Laser Powder Bed Fusion. Mater. *Sci Eng*. A 2025, 946, 149093.
11. Romero, J.; Preuss, M.; Quinta da Fonseca, J. Capturing the Texture Changes in a Zirconium Alloy During the Allotropic Phase Transformation. *Scr Mater*. 2009, 61, 399–402.
12. Cacuci, D.G., Ed. Handbook of Nuclear Engineering: Vol. 1: Nuclear Engineering Fundamentals; Vol. 2: Reactor Design; Vol. 3: Reactor Analysis; Vol. 4: Reactors of Generations III and IV; Vol. 5: Fuel Cycles, Decommissioning, Waste Disposal and Safeguards; Springer Science & Business Media: Berlin/Heidelberg, Germany, 2010.
13. Na, T.-H.; Na, S.-J.; Park, Y.-W. A Study on Characteristics of End Plug Resistance Welding Process in Nuclear Fuel Rods by Experiment and Numerical Simulation. *Int J Adv Manuf Technol*. 2018, 98, 2241–2255.
14. Kumar, N.A.P. Kiran; Szpunar, J.A.; He, Z. Microstructural Studies and Crystallographic Orientation of Different Zones and δ-Hydrides in Resistance Welded Zircaloy-4 Sheets. *J Nucl Mater*. 2011, 414, 341–351.
15. Burgers, W.G. On the Process of Transition of the Cubic-Body-Centered Modification into the Hexagonal-Close-Packed Modification of Zirconium. *Physica* 1934, 1, 561–586.
16. Joung, C.; Ahn, S.; Hong, J.; Kim, K. Development of TIG Welding System for a Nuclear Fuel Test Rig. In Proceedings of the KNS 2014 Spring Meeting, Gwangju, Korea, 30–31 May 2013; p. 3.
17. Silva, C.M.; Leonard, K.J.; Van Abel, E.; Geringer, J.W.; Bryan, C.D. Investigation of Mechanical and Microstructural Properties of Zircaloy-4 under Different Experimental Conditions. *J Nucl Mater*. 2018, 499, 546–557.
18. Magwentshu, N. Response of Zirconium-1.5% Sn to Autogenous Gas Tungsten Arc Welding. Master's Thesis, University of Pretoria, Pretoria, South Africa, 2018.
19. Da Silva, J.R.; Soares, B.F.S.; Luis; Alexandre, R. Methodology for the Development of the Welding Process of Fuel Rod End Plug, Applying Factorial Design and Analysis of Experiments. In Proceedings of the INAC 2019: International Nuclear Atlantic Conference - Nuclear New Horizons: Fueling Our Future, Santos, Brazil, 21–25 October 2019; pp. 4971–4983.